Bhatta *et al. Journal of Materials Science: Metallurgy* (2026) 1:13
https://doi.org/10.1007/s44492-026-00014-0

RESEARCH Open Access

Severe plastic deformation of powder-metallurgy CrMnFeCoNi alloy: Microstructure evolution and deformation mechanisms

Laxman Bhatta[1,2], Benji Roush[1,2], Tamara D. Koledin[1,2], Joshua D. Norton[3], Si-Yeon Lee[4], Jae-il Jang[4], Melissa K. Santala[1,2], Klaus-Dieter Liss[3] and Megumi Kawasaki[1,2*]

Abstract

Severe plastic deformation is well recognized for processing ultrafine-grained metals, and high-pressure torsion (HPT) is among the most effective techniques for achieving significant grain refinement at ambient temperature. By combining severe hydrostatic pressure with intense plastic shear straining, this study demonstrates the use of HPT for manufacturing fully dense bulk nanostructured metals directly from powder material. In this preliminary work, pre-alloyed CrMnFeCoNi high-entropy alloy (HEA) powders were processed via HPT. After 15 turns under 6 GPa at room temperature, the consolidated bulk sample reached 99.7% of the theoretical density, with a refined grain size of ~30 nm across both the disk center and edge. Vickers microhardness exhibited a homogeneous distribution exceeding 500 H_V, and micromechanical properties were evaluated using nanoindentation. The measured mechanical properties and microstructural parameters were used to estimate the diffusion coefficient of the nanostructured HEA under plastic deformation during nanoindentation. Lattice defect evolution with increasing HPT turns was assessed by X-ray diffraction analysis. While the results are compared with earlier reports on cast CrMnFeCoNi HEA processed by HPT, particular emphasis is placed on the temperature increase during powder consolidation, which differs from bulk processing. This study demonstrates an HPT-based powder metallurgy route for producing nanostructured metals without external heating and advances understanding of plastic deformation in nanostructured CrMnFeCoNi HEA.

Keywords High-entropy alloy, Grain boundary diffusion, High-pressure torsion, Nanostructure, Powder consolidation

Introduction

Blending multiple elements in near-equal proportions increases configurational entropy, suppresses brittle intermetallic phases, and enables compositionally complex alloys, including single-phase high-entropy alloys (HEA), opening new frontiers in alloy design and materials discovery (Cantor et al. 2004; Yeh et al. 2004; George et al. 2019). Currently, the fabrication of bulk HEA relies predominantly on conventional liquid-state processing, resulting in a microstructure often coarse and heterogeneous, requiring additional post-processing (Zhang et al. 2014; Pickering and Jones 2016; Miracle and Senkov

*Correspondence:
Megumi Kawasaki
megumi.kawasaki@oregonstate.edu
[1]School of Mechanical, Industrial and Manufacturing Engineering, Oregon State University, Corvallis, OR 97331, USA
[2]Materials Science Program, Oregon State University, Corvallis, OR 97331, USA
[3]University of Tennessee – Oak Ridge Innovation Institute, Knoxville, TN 37996, USA
[4]Division of Materials Science and Engineering, Hanyang University, Seoul 04763, Republic of Korea

2017). Alternatively, mechanical alloying and powder metallurgy (spark plasma sintering, hot pressing, hot isostatic pressing) (Zhang et al. 2024; Oketola et al. 2025), thermomechanical processing (forging, rolling, plastic forming) (Huang et al. 2024), and additive manufacturing (AM) (Chen 2024), are currently available for manufacturing bulk HEA. However, these thermal treatments during or after manufacturing frequently lead to grain coarsening, oxidation, and undesirable segregations (Chen et al. 2018; Kuzminova et al. 2021; Zamani et al. 2022; Dinita et al. 2023), resulting in compromised mechanical properties compared to those of their cast or wrought counterparts that are nanostructured by severe plastic deformation (Zhao et al. 2021a).

High-pressure torsion (HPT) has been widely applied to a variety of engineering metals and alloys as a post-manufacturing severe plastic deformation technique to produce bulk nanostructured metals (Valiev et al. 2006, 2016). A recent review shows strong interest in producing nanostructures in HEA by HPT, specifically those with face-centered cubic (f.c.c.) crystal structure (Chandan et al. 2026). The HPT process combines extreme hydrostatic pressure P and severe shear strain γ by torsion, offering unique severe plastic deformation of solids to achieve microstructural refinement. Specifically, the microstructure refinement occurs due to a severe shear strain imposed by the process, $\gamma = 2\pi rN/h$, where r is the radial distance from the disk center, N is the number of rotations, and h is the disk thickness (Zhilyaev and Langdon 2008). But this estimates only the surface-parallel planes of the samples. The fact is that the formation of a unique turbulent flow of solids occurs in the bulk volume during HPT, resulting in a rolling of vortices exhibiting localized areas with different levels of shear, as demonstrated by the finite element method (FEM) over the sample vertical cross-section (Kulagin et al. 2017). This led to the idea of applying HPT to mix and bond metal plates and powders for introducing hybrid nanostructured materials (Valiev et al. 2024).

Under HPT processing, fast shear deformation is concentrated near the sample surfaces, while gradual shear straining occurs in the bulk interior. This non-uniform deformation often evolves into vortex-like flow patterns along the plane normal to the torsional shear axis (Cao et al. 2010, 2011). While this behavior is attributed to a solid-state shear instability within bulk solids, it develops at the interfaces between separate solids under intense shear or sliding conditions and is characterized by the formation of interfacial vortices (Kulagin et al. 2018; Beygelzimer et al. 2021, 2023). Such vortex-driven material flow promotes the solid-state bonding of both similar and dissimilar bulk metals during HPT (Han et al. 2020; Hernández-Escobar et al. 2021). Thus, by applying powder metallurgy to HPT, severe shear interactions between individual powders or powder clusters are expected to trigger plastic instability, producing extensive regions of refined, complex phase mixtures and initiating interparticle bonding. Pioneering work in powder metallurgy–based HPT, had started much earlier (Korznikov et al. 1991; Valiev et al. 1996), and has recently been demonstrated as an effective route for producing bulk nanostructured HEA, using both pre-alloyed powders (Asghari-Rad et al. 2020, 2021; Son et al. 2022) and mixtures of pure elemental powders (Kulagin et al. 2017; Kilmametov et al. 2019; Stückler et al. 2021), and even HPT-alloying on f.c.c. HEA (Chandan et al. 2026). However, research on manufacturing bulk nanostructured HEA remains at an early stage, with many aspects still poorly understood, including the resulting nanostructure and defect states, as well as the thermally activated diffusion processes governing powder compaction and nanostructuring.

Accordingly, this work aims to demonstrate a new capability of the HPT process to enable concurrent room-temperature powder compaction and nanostructuring, and to systematically characterize the resulting microstructure and micro-mechanical properties of the nanostructured CrMnFeCoNi HEA. Special emphasis is placed on quantifying the temperature rise during HPT processing of powder compacts, identifying the micro-mechanical deformation mechanisms of the nanostructured HEA, and estimating the grain boundary diffusivity of the HEA during HPT up to 15 turns, as well as during post-manufacturing nanoindentation-induced plastic deformation at room temperature.

Experimental material and procedures

Pre-alloyed powder of a near-equiatomic single-phase CrMnFeCoNi alloy was purchased from MSE Supplies LLC. The nominal chemical composition in wt.% was 17.92 Cr, 19.94 Fe, 22.58 Co, 20.28 Ni, and bal. Mn. The powder contained 589 ppm oxygen and 222 ppm nitrogen, and the size distribution of the powders ranged from 15 to 53 μm. The initial powder morphology was characterized using scanning electron microscopy (SEM), and compositional analysis was performed through energy-dispersive X-ray spectroscopy (EDS). Figure 1 summarizes the powder compaction process using HPT. Approximately 2.5 g of powder was first pre-compacted into a pellet with a diameter of 10 mm and a height of 3–4 mm using a manual pellet press under a uniaxial pressure of 150–200 MPa for ~4 h. Pre-compacted pellets were subsequently processed by HPT under a compressive pressure of 6 GPa for 1, 2, 5 and 15 turns at a torsional speed of rotation of $\omega = 1$ rpm at room temperature. The temperature during HPT processing was

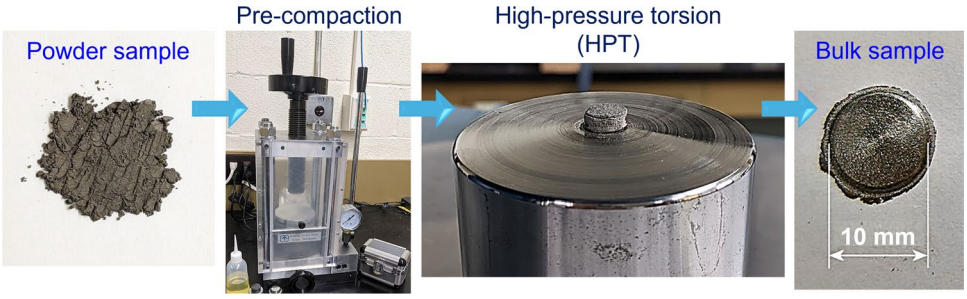

Fig. 1 An illustration of the powder compaction process in HPT. From left, initial powder sample, pre-compaction process using a pellet press, HPT process of the pellet, and the HPT-consolidated disk sample

monitored using a thermocouple inserted into a hole in the upper anvil, located 5 mm from the sample during processing.

The microstructures at the center and at the edge, 4 mm away from the center, on the mid-height plane of the HPT-consolidated disk sample after 15 turns were characterized using transmission electron microscopy (TEM). The TEM samples were prepared using a focused ion beam (FIB) in a Helios 650 ultra-resolution dual-beam field-emission gun (FEG) SEM. Initial milling was performed at 30 keV, followed by successive polishing steps from 5 keV to 0.5 keV. Bright-field TEM images were collected using a FEI Titan FEG TEM operated at 200 keV. Compositional analysis was carried out by collecting EDS data in scanning TEM (STEM) mode.

The densities of the HPT-consolidated samples were measured using a helium gas pycnometer, Micrometrics AccuPyc II 340 Gas Pycnometer. Entire disks were measured without sectioning. The sample volume was determined by helium gas displacement, and the density was calculated from the measured mass and volume. Each disk was evaluated 10 times to ensure statistical reliability. Further microstructural analysis was conducted using the X-ray diffraction (XRD) technique. XRD measurements were performed over the slightly polished surface of the HPT-consolidated disks as well as the initial powders using a PANalytical Aeris diffractometer with Cu–K_α radiation in a Bragg–Brentano geometry. Diffraction patterns were collected with a step size of 0.02° and a scanning speed of 7.95° min^{-1}.

The Vickers microhardness distribution along the diameter of each HPT-consolidated HEA disk was evaluated using a microhardness tester, Mitutoyo HM-200. The hardness distribution of each disk was obtained by averaging at least three line-scan measurements with a step size of 300 μm across the diameter on the vertical cross-sectional plane. Each disk was sectioned into two semi-circular halves by electrical discharge machining (EDM), mounted, and mechanically polished to obtain a mirror-finished vertical cross-section surface. All hardness measurements were conducted under an applied load of 300 gf with a dwell time of 15 s. The local micro-mechanical responses near the disk edges of the HPT-consolidated HEA disks were characterized by nanoindentation using a Nanoindenter-XP system. Indentations were performed with a three-sided pyramidal Berkovich diamond tip having a centerline-to-face angle of 65.3°. At a given measurement location, more than 20 indents were applied to ensure statistical reliability. All tests were carried out under a fixed maximum load of P_{max} = 50 mN, applied at constant indentation strain rates $\dot{\varepsilon}_i$ of 0.0125, 0.025, 0.05, and 0.1 s^{-1}. These loading rates correspond to equivalent representative strain rates of $\dot{\varepsilon}$= 1.25×10^{-4}, 2.5×10^{-4}, 5.0×10^{-4}, and 1.0×10^{-3} s^{-1}, respectively, as determined using an empirical relationship reported elsewhere (Wang et al. 2010; Choi et al. 2011).

Results

Initial microstructure of pre-alloyed HEA powder

Figure 2(a) shows an SEM image of a representative area of the powder particles (left) along with the surface of the particle from the yellow-boxed region and corresponding SEM–EDS elemental mapping of the initial pre-alloyed CrMnFeCoNi HEA powder. The majority of the pre-alloyed powder particles have a near spherical shape, with surface morphology showing a dendrite structure developed during the gas atomization process, and a homogeneous distribution of elements. By contrast, an EDS measurement revealed an inhomogeneous elemental distribution, specifically the depletion of Mn and Fe, in a powder particle located at the upper-left corner of the SEM image and captured by the dotted regions in the corresponding elemental maps in Fig. 2(b).

Microstructure of bulk HEA after powder consolidation via HPT

The densities of the pre-compacted powders before HPT processing and the samples after consolidation by HPT were measured, and the results are shown on the left in Fig. 3. The theoretical density of the equiatomic CrMnFeCoNi alloy is 7.964 g cm^{-3} (Gianelle et al. 2022). The pre-compacted specimen before HPT (N = 0) exhibits a density of 6.50 ± 0.01 g cm^{-3}, corresponding to 81.6% of the theoretical density. After one HPT turn, the density

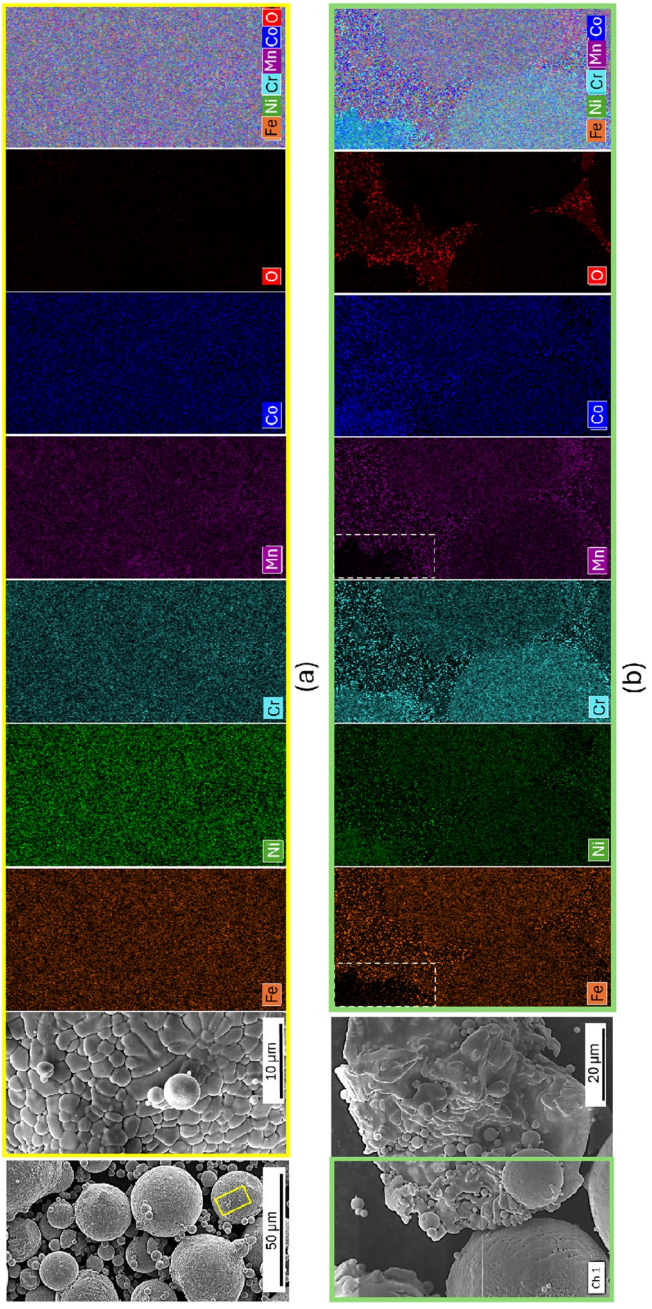

Fig. 2 **a** SEM image of the powders (left) along with the powder surface from the yellow-boxed region and corresponding SEM–EDS elemental mapping of the initial pre-alloyed HEA powder. **b** Representative powder particle showing localized depletion of Mn and Fe with an SEM image and corresponding SEM–EDS elemental mapping

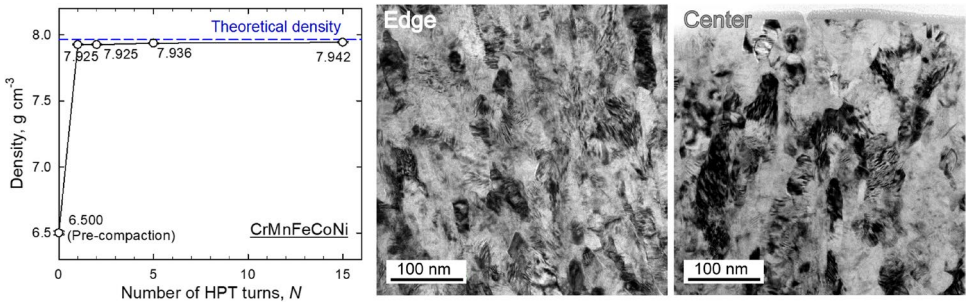

Fig. 3 (left) Density evolution from pre-compaction to increasing numbers of HPT turns, and (right) Bright-field TEM images at the edge and center of the HPT-consolidated CrMnFeCoNi alloy after 15 turns

increases to 7.925 ± 0.001 g cm^{-3}, or about 99.5% of the theoretical density, and increases slightly further to about 99.7% after 15 turns.

Representative TEM images taken from the edge and center of the disk sample are shown on the right in Fig. 3 for the HPT-consolidated CrMnFeCoNi HEA after 15 turns. The disk was well consolidated without any visible pores, and the microstructure achieved is similar between the edge and the center of the disk. The achieved grain size is ~30 nm from both regions, while some grain boundaries that flow along the shear direction are visible at the disk edge. For reference, the as-cast and homogenized equiatomic CrMnFeCoNi HEA showed saturated refined grain sizes of ~25 nm under 6 GPa (Mohammadi et al. 2022) and 50 nm under 7.8 GPa (Schuh et al. 2015; Skrotzki et al. 2020) through HPT at room temperature. It implies that powder consolidation via HPT demonstrates the feasibility of effective grain refinement, similar to conventional bulk metal processing via HPT.

The TEM–EDS results obtained at the disk edge of the CrMnFeCoNi alloy after 15 HPT turns show reasonable homogeneity in the elemental distributions of Cr, Mn, Fe, Co, Ni, and O, with no evidence of elemental depletion or segregation (see *Supplementary* Fig. 1). The mid-thickness plane of an HPT-processed disk, where the present TEM characterization was conducted, receives lower effective shear strain than the disk surfaces (Kawasaki et al. 2023; Reis et al. 2024), as recently demonstrated during solid-state mixing of Al and Mg plates processed by HPT (Wu et al. 2024). Importantly, such nanoscale chemical homogeneity could only be resolved at the length scales accessible by TEM and was not detectable using SEM-based characterization techniques (Wu et al. 2024). Nevertheless, the several regions observed at the disk edge showed homogeneous elemental distribution of the solid CrMnFeCoNi alloy.

An oxide phase of spinel compound $MnCr_2O_4$ with an over 200 nm size was observed at the disk edge (see *Supplementary* Fig. 2). The formation of such contamination-related oxides and carbides enriched in Mn and Cr is commonly observed in HEA, especially after annealing, where Mn and Cr are likely to create oxides easily due to the low-energy oxide formation in this particular HEA elemental combination (Christofidou et al. 2018; Liu et al. 2023; Gwalani et al. 2024). TEM-EDS analysis recorded outside of the oxide phase region shows a near-equiatomic distribution of the constituent HEA elements with measured compositions in at.% of 21.8 Cr, 18.2 Mn, 17.7 Fe, 18.5 Co, 18.6 Ni, and 5.2 O. It indicates increased content of O in the bulk HEA through the powder consolidation by HPT.

The results of STEM–EDS characterization conducted at the disk center are presented in Fig. 4. The EDS elemental mapping of the region in the high-angle annular dark field (HAADF) STEM image shown on the left was analyzed, including individual and combined elemental distributions, as well as the elemental profile obtained from an EDS line scan displayed on the combined elemental map. While the HAADF STEM image reveals an ultrafine-grained microstructure, consistent with that shown in Fig. 3, the EDS maps identify distinct compositional heterogeneities. Specifically, two elongated, thin bands enriched in Cr, Co, and Ni are observed in the elemental maps, which are also clearly resolved in the elemental intensity profiles. The elongated layers enriched in Cr, Co and Ni, but depleted in Mn and Fe, exhibit layer widths ranging from 10 to 60 nm. The thin bands are attributed to a refined region associated with nonuniform elemental distributions in the initial powder, as shown in Fig. 2(b). However, these features are observed only at the disk center and not at the edge, indicating that the higher accumulated shear strain of ~ 600 at the disk edge after 15 HPT turns effectively dissolved or fragmented the non-uniform regions, resulting in a more uniform elemental distribution.

XRD line profiles obtained from slightly polished disk surfaces are shown in Fig. 5 for both the HPT-consolidated CrMnFeCoNi HEA up to 15 turns and the initial pre-alloyed powder. All of these exhibit a single f.c.c. structure, while XRD has a limited detection sensitivity for minor or nanoscale phases. Because of nanostructuring by HPT, the consolidated HEA shows significant peak

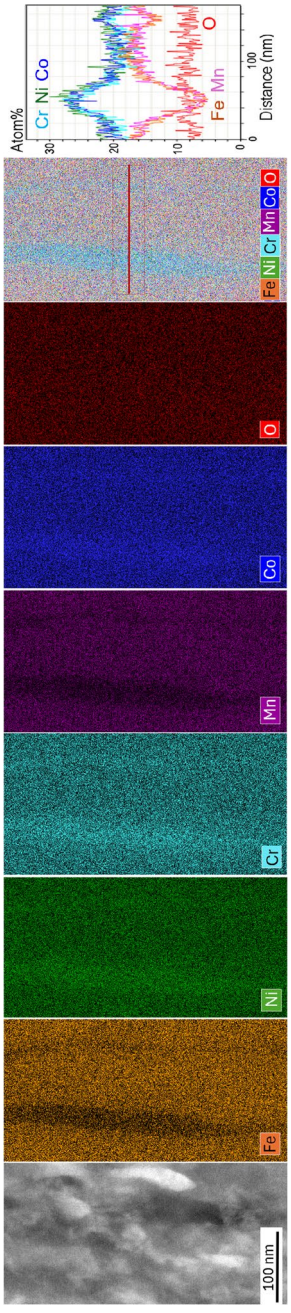

Fig. 4 STEM–EDS analysis at the disk center of the CrMnFeCoNi HEA after HPT for 15 turns. From left, a HAADF STEM image together with the EDS elemental maps, including the individual and combined elemental maps, and an elemental intensity profile obtained from an EDS line scan displayed on the combined elemental map

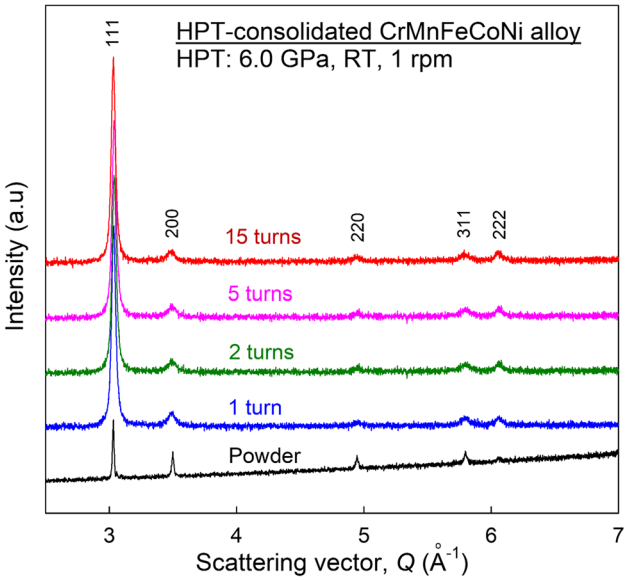

Fig. 5 XRD peak profiles for the HPT-consolidated CrMnFeCoNi HEA up to 15 turns and the initial pre-alloyed powders

broadening. This observation is consistent with earlier studies on equiatomic CrMnFeCoNi subjected to HPT, where no secondary phases were detected after 10 turns under 6 GPa (Shahmir et al. 2016).

Micro-mechanical behavior of HPT-consolidated nanostructured HEA

The estimated average hardness and its standard deviation across the disk diameters are shown in Fig. 6 for the nanostructured HEA after HPT powder consolidation for different numbers of turns. The evolution of hardness across the disk diameter of the HPT-consolidated HEA follows a typical pattern with hardening (Kawasaki 2013), driven primarily by grain refinement and strain hardening, as indicated by the maintenance of a single phase, as seen in the XRD results in Fig. 5. After 1 and 2 turns of HPT, the hardness at the disk centers reached the hardness just above $H_V = 400$, while the disk edge reached around 480. Through 15 HPT turns, the hardness was saturated at $H_V = 507 \pm 5$ across the disk diameter. Overall, these findings confirm that powder consolidation and concurrent grain refinement by 15 turns of HPT yield a homogeneous microstructure. The achieved hardness of the nanostructured CrMnFeCoNi HEA produced via the room-temperature powder-metallurgy route is in agreement with the reported saturated hardness of $H_V \approx$ 510–520 of the same CrMnFeCoNi HEA in cast, followed by HPT (Schuh et al. 2015; Skrotzki et al. 2020; Chulist et al. 2022). Nevertheless, although similar hardness developments are observed in bulk metal processing, the direct transformation from particles to fully dense

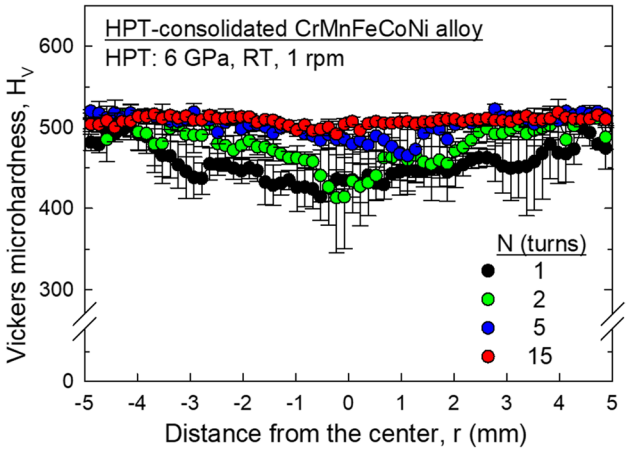

Fig. 6 Vickers microhardness variations along the disk diameter of the HPT-consolidated nanostructured CrMnFeCoNi HEA up to 15 turns

nanostructured metal with such high hardness represents a significant novelty.

While Vickers microhardness measurements can evaluate microstructural changes at the micron scale (Wu et al. 2026), it lacks sensitivity to atomic-scale features (Wu et al. 2024). To determine the micro-/nano-mechanical behavior of the nanostructured HEA after HPT powder consolidation, nanoindentation was applied at the edge of the processed disks. Figure 7 presents representative load–displacement (*P*–*h*) curves obtained at four equivalent strain rates of 1.25×10^{-4}, 2.5×10^{-4}, 5.0×10^{-4}, and 1.0×10^{-3} s^{-1} measured after HPT for (a) 1 turn and (b) 15 turns. A similar presentation of the curves for the disks after HPT for 2 and 5 turns is shown in *Supplementary* Fig. 3. The displacement responses are similar across the tested strain rate range after 1 HPT turn, and this behavior is maintained after 15 turns, although slightly lower displacements, indicating higher hardness, are observed at all strain rates. Moreover, comparison of the distributions obtained from 20 indentations reveals wider scatter in *h* at lower strain rates after 1 and 2 turns (see *Supplementary* Fig. 3), whereas the *P*–*h* curve distributions after 15 turns are consistent across all strain rates. The broader scatters in the *P*–*h* responses indicate microstructural inhomogeneity at the disk edges in the early stages of HPT processing. Such inhomogeneity is more readily captured at lower strain rates. Also, it agrees with the Vickers microhardness results at the disk edges after 1 and 2 turns, where larger error bars are observed compared with disks processed to higher HPT turns. In the regime of fully plastic flow state, the flow stress σ_f is characterized using Tabor's empirical correlation, $\sigma_f \approx H_N/3$, where H_N denotes the measured nanoindentation hardness (Oliver and Pharr 2011). The calculated flow stresses at different strain rates through nanoindentation are shown in Table 1.

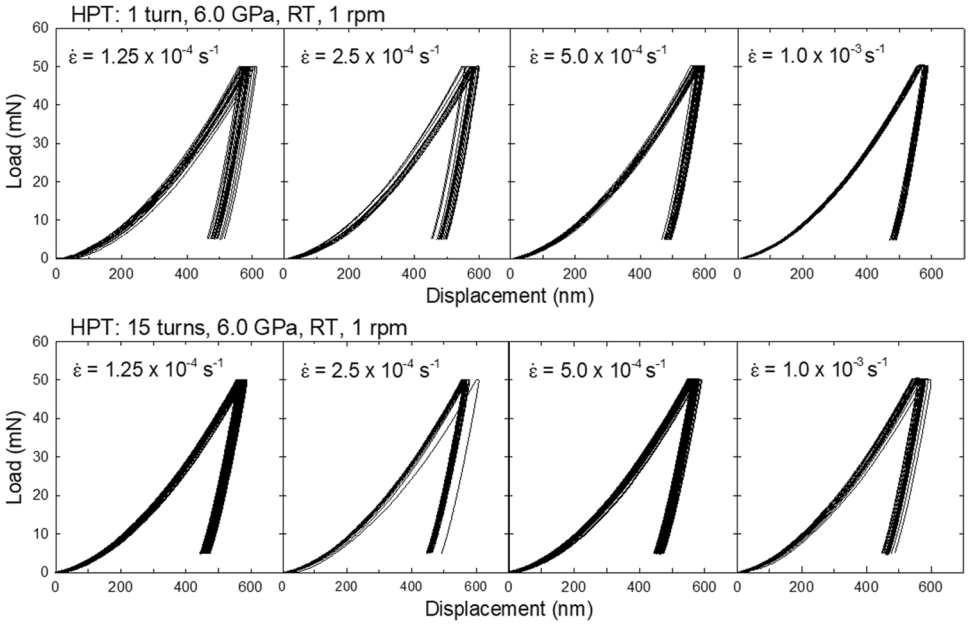

Fig. 7 Representative load–displacement (*P–h*) curves recorded by the nanoindentation method taken at the disk edges of HPT-consolidated nanostructured CrMnFeCoNi HEA after (upper) 1 turn, and (lower) 15 turns at four strain rates at 1.25×10^{-4}—1.0×10^{-3} s^{-1}

Table 1 Calculated flow stresses at different strain rates by nanoindentation of HPT-consolidated nanostructured CrMnFeCoNi HEA

	Number of HPT turns, *N*	Strain rate, $\dot{\varepsilon}$ (s^{-1})			
		1.25×10^{-4}	2.5×10^{-4}	5×10^{-4}	1×10^{-3}
Flow stress, σ_f (GPa)	1	2.05 ± 0.09	2.10 ± 0.10	2.12 ± 0.06	2.23 ± 0.06
	2	2.06 ± 0.07	2.14 ± 0.05	2.18 ± 0.09	2.23 ± 0.06
	5	2.12 ± 0.07	2.15 ± 0.08	2.22 ± 0.07	2.27 ± 0.05
	15	2.23 ± 0.06	2.27 ± 0.08	2.33 ± 0.08	2.37 ± 0.09

Discussion

A new model of temperature rise during HPT powder consolidation

The HEA powder consolidation using HPT processing at atmospheric temperature can benefit from the temperature rise due to friction between powders during the early stage of HPT consolidation, internal friction of the consolidated bulk, as well as friction between the anvils and the solid disk sample afterward. There have been several experimental and modeling efforts to build equations for estimating this temperature rise occurring during HPT. However, estimation may vary with different HPT setups, including materials and volumes of anvils, varying thermal conductivity and heat capacity (Figueiredo et al. 2012), different materials and torsion rate ω (Edalati et al. 2011), and the location of measurement from the sample (Hóbor et al. 2010), as well as different sample sizes and rotation speeds.

Two equations have been developed based on a similar concept estimating the temperature rise during HPT. The earlier simplified equation showing the temperature rise ΔT (K) is shown below using Ti alloy (Pereira et al. 2014),

$$\Delta T = \alpha\sigma_f\omega[1 + b\,(1 - exp(-t/c)] \quad (1)$$

where σ_f is the flow stress of the sample in MPa, t is the processing time in s, and α is the heat generation coefficient in K MPa^{-1} s, b is a dimensionless constant, and c is a relaxation time coefficient with units in s. Most HPT processing on the bulk disk and plate samples shows a temperature rise followed by the upper saturated temperature. For tool-steel anvils rotating at $\omega = 1$ rpm $= 2\pi/60$ rad $s^{-1} = 0.105$ s^{-1} and a sample with a radius of 5 mm and a thickness of 0.8 mm, the model estimates $b = 1.28$ and $c = 482$ s, and $\alpha = 0.22$ K MPa^{-1} s at the earlier stage of HPT, followed by $\alpha = 0.5$ K MPa^{-1} s under the saturation condition. This model was validated by experiments using Ti alloy with different sample sizes and volumes.

Another equation similar to Eq. (1) but in a simplified form is given below (Edalati et al. 2018),

$$\Delta T = \beta\sigma_f\omega[(1 - exp(-t/c)] \quad (2)$$

where both β is the heat generation coefficient with units K MPa^{-1} rpm^{-1}, and ω is in rpm. The thermal property of the sample is considered to have a marginal effect, while the critical parameter is the flow stress of the material, which is consistent in both Eqs. (1) and (2). In this report, $\beta = 0.017$ and $c = 2$ were applied and validated by experiments on Sn, Al, Ag, Cu and Ti for the early stage of HPT up to 1 turn under ω =1 rpm (Edalati et al. 2018).

Equations (1) and (2) establish similar semi-empirical models for the temperature rise upon HPT processing. Both models relate the temperature rise proportional to the flow stress σ_f of the material and the processing speed ω. The exponential function with an individual time scale c depends on the heat dissipation from the HPT specimen into the anvils, which further depends on the geometry, the position of the temperature sensor, and the thermal properties of the system, i.e., anvils. The experiments in the two reports differ significantly in the placement of the temperature sensor, namely 10 mm above the specimen in the bulk of the anvil (Pereira et al. 2014) and directly contacting a specimen (Edalati et al. 2011). Nevertheless, considering the conversion between rpm and s^{-1}, the reported parameters α and β are consistent, i.e., in the same order of magnitude.

The present HPT experiments employed a conventional, quasi-constrained setup. However, the powder metallurgy-based fabrication of bulk nanostructured HEA exhibited a distinct temperature rise. This behavior is displayed in Fig. 8, with three independent experimental trials indicated by solid lines. During the early stage of HPT up to ~100–150 s, ΔT increased more rapidly than predicted by the models in Eqs. (1) and (2). With continued processing up to 900 s that is corresponding to 15 turns, the HPT powder consolidation accompanied by nanostructuring exhibited a stable and sustained increase in ΔT.

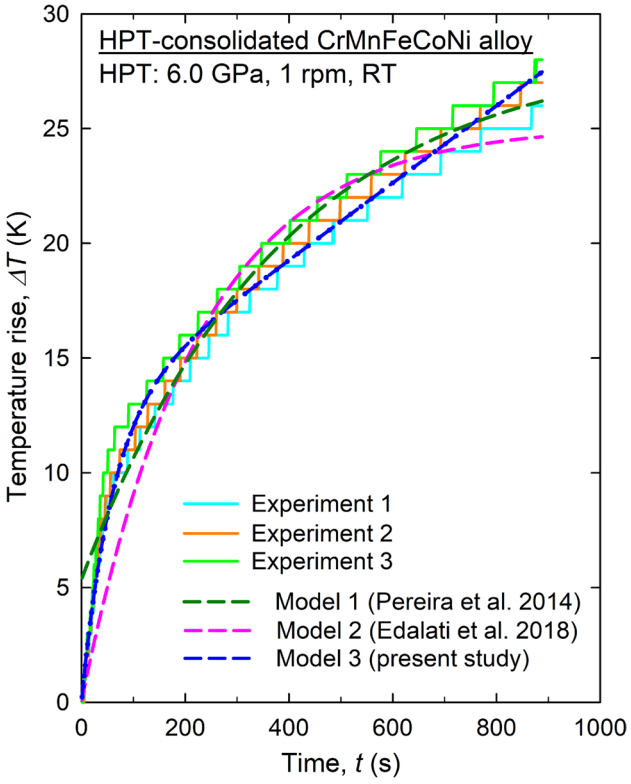

Fig. 8 Plot showing temperature rise with HPT processing time for the HEA powder consolidation by HPT for 15 turns under 6 GPa at 1 rpm = 2π/60 rad s^{-1} = 0.105 s^{-1}. Solid lines represent the three experimental datasets, while the calculated model relationships are shown as dotted curves

The green curve labeled *Model 1* in Fig. 8 was computed as the best fit to the experimental data 1–3 using Eq. (1) with the flow stress σ_f = 2.37 GPa of the HEA after 15 HPT turns at ω = 0.105 s^{-1}, taken from nanoindentation measurements at the highest strain rate (see Table 1). The fitting was performed using α = 0.0216 K MPa^{-1} s, b = 4.32, and c = 386 s. This model deviates from experimental data, particularly at the early stage of HPT. By contrast, the red dotted curve labeled *Model 2* in Fig. 8 was obtained using Eq. (2), again employing the nanoindentation-derived flow stress of the HEA after 15 turns. The best fit to the experimental data was achieved with β = 0.0106 K MPa^{-1} rpm^{-1} and c = 224 s. Nevertheless, this calculation also fails to capture the accelerated increase in ΔT during the early stage of HPT, nor does it reproduce the nearly constant rate of ΔT increase observed at later stages.

Accordingly, a new empirical equation is proposed, which is similar in form to Eq. (2) but includes an additional term analogous to Eq. (1), as given below:

$$\Delta T = \beta \sigma_f \omega \left[(1 - \exp(-t/c)\right] + kt \tag{3}$$

where k is a constant with units K s^{-1}. The blue dotted line labeled *Model 3* in Fig. 8 provides the best fit for the experimental data. The model parameters are β = 0.0053 K MPa^{-1} rpm^{-1}, c = 58 s, and k = 0.016 K s^{-1}, or equivalently β = 0.051 K MPa^{-1} s, c = 58 s, and k = 0.016 K s^{-1} when using ω in rad s^{-1} The parameters correspond to powder HEA consolidation by HPT for 15 turns under a pressure of 6 GPa, with the temperature sensor positioned ~5 mm above the sample. Further analysis incorporating a wider range of HPT turns, different HEA compositions, and varying angular velocities (ω) is required.

While the first two models indicate a saturation temperature after a characteristic time constant c, the new model asymptotically approaches a linear temperature increase with time, indicating different dissipation of heat, where *Models 1* and *2* may contain an infinite heat sink e.g. active cooling with different volume of anvils, while *Model 3* configures an isolated anvil, from which heat does not easily dissipate into the environment and temperature just increases with the produced heat according to its heat capacity. This may also arise from differences in the powder processing conditions that *Model 3* was developed to match, compared with those assumed in *Models 1* and *2*. Thus, the new model for estimating ΔT, proposed in Eq. (3), specifically captures the quick heating during the first 1–2 turns, equivalent to t up to 120 s, and the maximum recorded temperature rise

in this study of $\Delta T > 25$ K for powder compaction and nanostructurization through 15 HPT turns.

Lattice defects and nanostructure

The XRD peak profiles shown in Fig. 5 were analyzed using the classical Williamson-Hall (W–H) method, enabling separation of peak broadening from the influences of crystallite size d_{XRD} and microstrain $\Delta\varepsilon$, with the following relationship,

$$\Delta Q = K\frac{2\pi}{d_{XRD}} + \Delta\varepsilon Q \tag{4}$$

where the peak position $Q = 2\ k\ \sin(\theta)$ with wavevector $k = 2\pi/\lambda$, Bragg angle θ, and wavelength λ, and K is a shape factor, equal to 0.9 for spherical particles (Patterson 1939). Figure 9(a) shows a W–H plot taking full width at half maximum (FWHM), ΔQ, versus scattering vector, Q, for the pre-alloyed HEA powders and the consolidated HEA by HPT for 15 turns. Other samples consolidated by HPT for small numbers of turns are shown in *Supplementary* Fig. 4. The data from different Q of f.c.c. peaks for the initial HEA powders showed that the data fit Eq. (4) nicely, as shown in the black line, so that $d_{XRD} = 843$ nm and $\Delta\varepsilon = 0.00431$ were estimated. By contrast, the disk after 15 turns shows the scattered data from the classical W–H relationship due to the lattice strain anisotropy around dislocations (Karato 2009) occurring through severe plastic deformation that has been observed often after HPT processing on bulk metals, including 316L stainless steels and CrFeCoNi f.c.c. alloys (Han et al. 2021; Liu et al. 2023). While the method can be used by taking slip planes, for instance, 111 and 222 for f.c.c. crystals (Han et al. 2021; Kawasaki et al. 2022) or using the diffraction technique that enables the reflection peaks through high Q (Lee et al. 2025) so as not to overestimate d_{XRD} and $\Delta\varepsilon$, it is reasonable to further consider the strain anisotropy in the severely strained HEA after HPT.

To account for the lattice strain anisotropy, a modified W–H method is applied for all samples including the initial powder. This method incorporates an average dislocation contrast factor $\overline{C}$ and the Wilkens dislocation arrangement parameters M into the broadening relation, as shown in Eq. (5);

$$\Delta Q = K\frac{2\pi}{d_{XRD}} + \left(\frac{M\mathbf{b}^2}{4}\right)\rho^{\frac{1}{2}}Q^2\overline{C} \tag{5}$$

where $M = R_e\,\rho^{1/2}$ is a dimensionless unit that characterizes the dislocation dipole, R_e is the effective outer cutoff radius of dislocations in a random dislocation distribution (Wilkens 1970), ρ is the dislocation density, and **b** is the Burgers vector. The average dislocation contrast factor $\overline{C}_{hkl}$ at the *hkl* reflection can be estimated by,

$$\overline{C}_{hkl} = \overline{C}_{h00}(1 - qH^2) \tag{6}$$

where $\overline{C}_{h00}$ is the average contrast factor of h00 reflection, q represents the dislocation type (edge or screw) and $H^2 = (h^2k^2 + k^2l^2 + l^2h^2)/(h^2 + k^2 + l^2)^2$ is the orientation factor (Ungár et al. 1998). Theoretical values of q were calculated by the relation developed for f.c.c. crystals (Ungar et al. 1999) as shown below,

$$q = a\,[1 - \exp(-A_i/b)] + cA_i + d \tag{7}$$

where $A_i = 2C_{44}/(C_{11}\text{-}C_{12})$ is an elastic anisotropy factor estimated by the elastic stiffness constants of $C_{11} = 172.1$ GPa, $C_{12} = 107.5$ GPa and $C_{44} = 92.0$ GPa for CrMnFeCoNi HEA (Wu et al. 2014), and *a, b, c* and *d* are constant for edge and screw dislocations for f.c.c. crystals (Ungar et al. 1999).

The modified W–H plot is shown in Fig. 9(b) for the powder sample and the disk after HPT for 15 turns. The

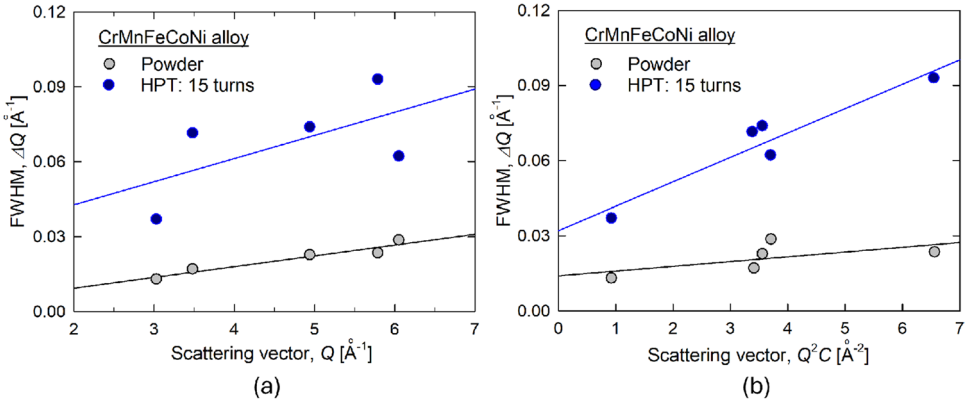

Fig. 9 **a** Classical Williamson-Hall plot, and **b** modified Williamson-Hall plot for the initial CrMnFeCoNi powders and the HPT-consolidated HEA disk for 15 turns

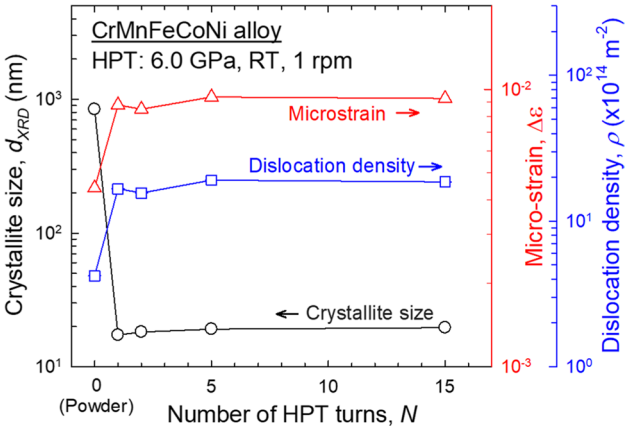

Fig. 10 The evolution of microstructural parameters of crystallite size d_{XRD}, microstrain $\Delta\varepsilon$, and dislocation density ρ with increasing HPT turns N for CrMnFeCoNi HEA powder consolidation

other samples after HPT were also analyzed through the Modified W–H method, and the corresponding plots are shown in *Supplementary* Fig. 4. This refinement process yields well-fitted linear relationships, especially for the HEA after 15 HPT turns, with a quality comparable to that of the initial powders before plastic deformation. This modified W–H analysis provides more reliable estimates of the microstructural parameters of domain size d_{XRD}, microstrain $\Delta\varepsilon$, and dislocation density ρ. These parameters are plotted in Fig. 10 against the number of HPT turns N, where the results for the initial powders are shown at $N=0$. The numerical values are summarized in Table 2. The results show nanostructuring of the HEA reaching d_{XRD} ~20 nm occurs with increasing dislocation density of $\rho > 10^{15}$ m^{-2} and a two-fold increase in microstrain even after 1 HPT turn, and these stay almost constant through 15 turns. Although the estimated dislocation density in the present study is lower than the reported values of ~10^{16} m^{-2} for bulk CrMnFeCoNi HEA processed by HPT (Skrotzki et al. 2020; Heczel et al. 2017), the minimum achieved domain size of d_{XRD} ~20 nm and the grain size determined by the microscopy technique of d ~ 30 nm after HPT (Heczel et al. 2017) are consistent with those observed in the present HPT-powder consolidated HEA. The estimated $\mathbf{b} = 2.54$ Å for all sample conditions corresponds to a lattice constant of $a \sim 3.59$ Å for the HEA, which remains essentially unchanged across all conditions, while a slight lattice expansion is calculated after HPT powder consolidation.

Micro-mechanical behavior of powder-consolidated bulk nanostructured HEA

Nanoindentation is well-suited for evaluating local mechanical properties and their variations by probing small material volumes at specific locations, enabling accurate measurement of micro-mechanical properties in the presence of microstructural gradients arising from shear strain heterogeneity during HPT processing (Kawasaki et al. 2017). An earlier review summarized recent progress in the use of nanoindentation to understand the micro-mechanical responses of nanostructured f.c.c. HEA (Lee et al. 2023).

The nanoindentation results are analyzed to determine rate-sensitive parameters such as the strain-rate sensitivity m, and to identify thermally-activated plastic deformation mechanisms by calculating the activation volume V^*. For indentation conducted at a nominally constant strain rate, the indentation strain rate is defined as $\dot{\varepsilon}_i = (\mathrm{d}h/\mathrm{d}t)/h$, with h corresponding to the penetration depth and t representing time. At fixed values of strain ε and temperature T, the strain-rate sensitivity m and the effective activation volume V^* are obtained from the rate dependence of hardness according to the relations below (Choi et al. 2013):

$$m = \left(\frac{\partial \ln \sigma_f}{\partial \ln \dot{\varepsilon}}\right)_{\varepsilon,T} = \left(\frac{\partial \ln(H_N/3)}{\partial \ln(0.01\,\dot{\varepsilon}_i)}\right)_{\varepsilon,T} \tag{8}$$

$$V^* = \sqrt{3}kT\left(\frac{\partial \ln \dot{\varepsilon}}{\partial \sigma_f}\right)_{\varepsilon,T} = \sqrt{3}kT\left(\frac{\partial \ln(0.01\,\dot{\varepsilon}_i)}{\partial (H_N/3)}\right)_{\varepsilon,T} \tag{9}$$

where k is Boltzmann's constant.

The estimated m and V^* derived from the nanoindentation datasets shown in Fig. 7 and *Supplementary* Fig. 3 for the nanostructured HEA are summarized in Fig. 11 as a function of the number of HPT turns. The strain rate sensitivity m decreases with increasing HPT turns, however, it remains in the range of ~0.03–0.04 across the grain or crystallite sizes shown in Fig. 10. These m values

Table 2 The estimated numerical microstructural parameters of crystallite size d_{XRD}, microstrain $\Delta\varepsilon$ with linear regression parameter α, and dislocation density ρ with increasing HPT turns N for CrMnFeCoNi HEA powder consolidation

Material		Linear regression parameter α (Å^{-1})	Crystallite size d_{XRD} (nm)	Microstrain $\Delta\varepsilon$	Dislocation density ρ (m^{-2})
Powder		0.0007 ± 0.003	843	0.0043 ± 0.001	4.22×10^{14}
Bulk via HPT consolidation	1 turn	0.036 ± 0.01	17	0.0087 ± 0.006	1.67×10^{15}
	2 turns	0.034 ± 0.005	18	0.0084 ± 0.005	1.56×10^{15}
	5 turns	0.032 ± 0.005	19	0.0093 ± 0.005	1.91×10^{15}
	15 turns	0.032 ± 0.007	20	0.0092 ± 0.006	1.86×10^{15}

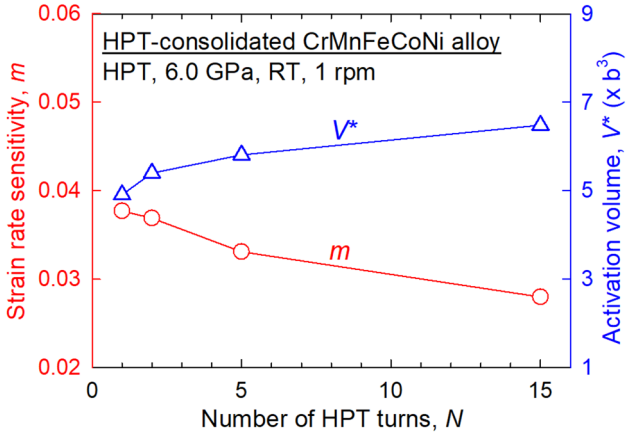

Fig. 11 Variation of strain rate sensitivity m and activation volume V^* for the powder consolidated HEA after HPT for 1 to 15 turns under 6 GPa

are higher than those for Ni and Ni-based alloys showing $m \sim 0.02$–0.03 and are comparable to those of f.c.c. CrMnFeCoNi and AlCrFeCoNi high-entropy alloys (Zhao et al. 2021b). Previous studies report a decrease in m for as-cast CrMnFeCoNi HEA from ~0.038 to ~0.031 after ¼ turn and to < 0.03 between 1/2 and 2 HPT turns (Lee et al. 2015). Although the m value of this present study declines gradually with increasing plastic deformation, its absolute value remains within the range reported in earlier studies. This suggests that powder metallurgy through HPT is a promising route for manufacturing bulk nanostructured HEA with enhanced plasticity, similar to conventional bulk HPT processing.

The value of V^* varies by orders of magnitude depending on different rate-controlling processes of materials (Zhu et al. 2007). Typical values are on the order of 10^2–10^3 $\mathbf{b}^3$ for dislocation glide in f.c.c. metals (Conrad 2003), ~ 10 $\mathbf{b}^3$ for grain boundary sliding (Conrad 2007) and ~ $\mathbf{b}^3$ to below 10 $\mathbf{b}^3$ for diffusion-mediated deformation processes, either along grain boundaries or through the crystalline lattice (Conrad 2003; Frost and Ashby 1982). The computed V^* values in the present study range from 5.0 $\mathbf{b}^3$ to 6.5 $\mathbf{b}^3$, implying that the dominant deformation mechanism in the nanostructured HEA is diffusion-controlled dislocation activity, particularly a grain-boundary diffusion-dominated process, where diffusion is much more pronounced in the nanocrystalline state, thus leading to grain-boundary sliding. In contrast, in bulk HEA subjected to grain refinement by HPT, the activation volume typically decreases slightly with increasing N as reported for CrMnFeCoNi HEA (Lee et al. 2015), while the observed V^* values remain within a similar range of ~6–8 $\mathbf{b}^3$.

The observed slight increase in V^* with increasing N may be attributed, at least in part, to the temperature rise during HPT as seen in Fig. 8, as similar increases in V^* were reported under elevated-temperature nanoindentation (Lee et al. 2018). While the present nanoindentation experiments were conducted at room temperature after HPT, the potential imprint of this thermal effect on the resulting microstructure should be considered. Nevertheless, the observed increase in V^* suggests a possible growing contribution of grain boundary–mediated deformation mechanisms, such as grain boundary sliding and diffusion creep, in the nanostructured HEA.

Grain boundary diffusivity in nanostructured HEA

The interpretation of the present results enables estimation of diffusivity through grain boundaries, thus grain boundary diffusivity D_{gb}, in the HPT-consolidated bulk nanostructured CrMnFeCoNi HEA during nanoindentation-induced plastic deformation at room temperature. D_{gb} in the post-consolidated HEA can be estimated under nanoindentation-induced plastic flow at $T = 298$ K. A recent work (Figueiredo et al. 2023) examined the effect of grain size on the flow stress by reconstructing the original rate equation (Langdon 1994), subsequently modified (Figueiredo and Langdon 2021) and further adapted to incorporate the mean linear intercept grain size d_l according to the approach (Thompson 1972). The plastic deformation in nanostructured materials, dominated by grain boundary sliding accommodated by grain boundary diffusion, as indicated by the present nanoindentation results, can be expressed as follows (Figueiredo et al. 2023):

$$\sigma_f = \sqrt{\frac{\sqrt{3}GkT}{2d_l \mathrm{b}^2} ln\left(\frac{\dot{\varepsilon} d_l^3}{2\delta D_{\mathrm{gb}}} + 1\right)} \qquad (10)$$

where G is the shear modulus, k is the Boltzmann constant, and δ is the grain boundary width that is often taken as ~2 **b**. The m value increases with increasing temperature, as implied in Eq. (8). When the grain size is stable, there will be higher strain-rate sensitivity at higher temperatures, ultimately leading to values of $m \sim 0.5$, then Eq. (10) is associated with the occurrence of conventional superplasticity. By contrast, Eq. (10) also works for ambient temperatures, as was shown with Al, Cu and other metals, where m is as low as 0.03 at ambient temperature, including room temperature, Eq. (10) fits reasonably well with the experimental results for ultrafine-grained conditions.

By contrast, the flow stress for HEA, specifically CrMnFeCoNi HEA, Eq. (10) can be modified to account not only for grain refinement strengthening but also for the significant contribution of solid-solution strengthening depending on the temperature of testing and processing (Laplanche et al. 2018). Such a modified approach, leading to the flow stress σ_f tested at room temperature for

ultrafine-grained CrMnFeCoNi HEA, has been reported (Figueiredo et al. 2022).

$$\sigma_f = \sigma_0 exp\left(-\frac{1}{0.51}\frac{RT}{\Delta E_b} ln\left(\frac{\dot{\varepsilon}_0}{\dot{\varepsilon}}\right)\right) + \sqrt{\frac{\sqrt{3}GkT}{2d_l \mathrm{b}^2} ln\left(\frac{\dot{\varepsilon} d_l^3}{2\delta D_{\mathrm{gb}}} + 1\right)} \quad (11)$$

where σ_0 is the intrinsic lattice friction stress at 0 K, ΔE_b is the activation energy barrier, and $\dot{\varepsilon}_0$ is a reference strain rate that this study takes 10^4 s^{-1} following the report (Laplanche et al. 2018). Equation (11) was shown to successfully describe the flow stress of nanostructured CrMnFeCoNi HEA over a wide temperature range from 77, 293 to 1073 K. In the present study, flow stress σ_f at specific strain rate $\dot{\varepsilon}$ is available from nanoindentation results, and applying $G = 80{,}424$ MPa at 298 K of CrMnFeCoNi (Laplanche et al. 2015), $\sigma_0 = 405$ MPa (Wu et al. 2014) and $\Delta E_b = 1.13$ eV consisting of 109 kJ mol^{-1} (Laplanche et al. 2018) for CrMnFeCoNi, and $\mathbf{b} = 2.54$ Å and $d_l = 30$ nm from the TEM analysis for the present CrMnFeCoNi HEA, D_{gb} of 1.4×10^{-17} – 9.0×10^{-17} $m^2 s^{-1}$. This further yields the apparent activation energy with $Q_{\mathrm{gb}} = 85$–93 kJ mol^{-1} for nanostructured CrMnFeCoNi at 298 K. It falls within a reasonable range with $Q_{\mathrm{gb}} \sim 50$ kJ mol^{-1} computed from the estimated activation enthalpy of ~0.5 eV at 298 K by nanoindentation (Lee et al. 2018) and a modeled Q_{gb} value of 90 kJ mol^{-1} at 300 K (Figueiredo et al. 2022), which confirms the conclusions received by nanoindentation of the micro-mechanical behavior of the nanostructured CrMnFeCoNi HEA under nanoindentation-induced plastic deformation through grain boundary diffusion.

Figure 12 summarizes the reported D_{gb} at various temperatures, including the present analysis for nanoindentation-induced plastic deformation at 298 K (green stars). Reference D_{gb} values for Ni diffusion in pure Ni (Divinski et al. 2010), Fe–40Ni (Kang et al. 2004), and CrFeCoNi and CrMnFeCoNi alloys (Vaidya et al. 2017) with all having coarse-grained microstructure are shown as dotted lines. Also included are reported D_{gb} for Co diffusion in coarse-grained CrMnFeCoNi HEA (Glienke et al. 2020) and ECAP-processed ultrafine-grained (UFG) CrMnFeCoNi HEA (Jiang et al. 2024), as well as Ni diffusion in UFG pure Ni after ECAP (Divinski et al. 2011) and additively manufactured (AM) CrMnFeCoNi HEA (Choi et al. 2020, 2024). The reference data were primarily derived from radiotracer measurements conducted at elevated temperatures.

The present analysis yields significantly higher values of D_{gb}, indicating much faster effective diffusivity during nanoindentation-induced plastic deformation. This enhancement can be attributed to the activation of fast diffusion paths associated with stress-assisted grain boundary diffusion and grain boundary sliding under the highly localized stress fields generated during nanoindentation at controlled strain rates (Li et al. 2002; Kirchheim 2007). Since the vacancy concentration in HPT-processed materials approaches thermally activated levels near the melting temperature (Liu et al. 2023; Čížek et al. 2019), it accelerates higher diffusivities even at ambient temperature. The dominance of these processes is further promoted by the nanostructured condition, where the high density of grain boundaries governs plastic deformation (Conrad 2003). On the other hand, the grain boundary δ width is an assumed parameter, which is based on thermally stabilized grain boundaries. In highly distorted HPT material, however, the manifold of the grain boundary is not smooth, i.e., non-equilibrium grain boundaries are reported with the widths about 1–2 nm (Sauvage et al. 2012) in SPD-processed materials. This results in δ being approximately two to three times higher, leading to an overestimation of D_{gb} in the present analysis. However, the resulting shift of D_{gb} toward lower values remains relatively small. Although this behavior

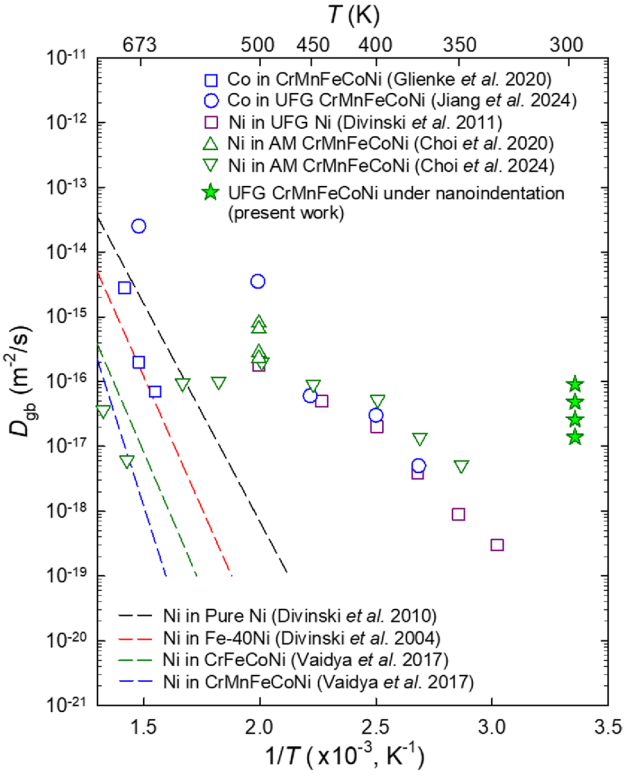

Fig. 12 Grain boundary diffusion coefficient D_{gb} at various temperatures estimated for nanoindentation-induced plastic deformation at 298 K (green stars). Reference D_{gb} values for Ni diffusion in pure Ni (Divinski et al. 2010), Fe–40Ni (Kang et al. 2004), and CrFeCoNi and CrMnFeCoNi alloys (Vaidya et al. 2017) are shown as dotted lines. Also included are reported Co diffusivity in coarse-grained CrMnFeCoNi HEA (Glienke et al. 2020) and ECAP-processed UFG CrMnFeCoNi HEA (Jiang et al. 2024), as well as Ni diffusivity in UFG pure Ni after ECAP (Divinski et al. 2011) and AM CrMnFeCoNi HEA (Choi et al. 2020, 2024)

contrasts with the commonly cited concept of sluggish diffusion in HEA, the present results demonstrated that nanostructure-promoted, grain boundary–mediated diffusion and deformation processes dominate plastic flow in HPT-consolidated CrMnFeCoNi HEA.

Summary and conclusions

(1) This study demonstrated the capability of powder metallurgy HPT at room temperature to manufacture bulk nanostructured HEA from pre-alloyed CrMnFeCoNi powders. The density increased significantly to 99.5% after 1 turn and ultimately reached 99.7% of the theoretical density of HEA after 15 HPT turns.

(2) The microstructure reached reasonably equiaxed grain sizes of 30 nm observed by TEM at both the disk center and edge after 15 HPT turns. While the elements were well distributed at the disk edge, CrCoNi-rich thin layers with widths of 10–60 nm remained at the disk center, originating from minor particles with that composition. After 15 HPT turns, the disk exhibited a homogeneous distribution of microhardness $H_V = 507 \pm 5$ across the disk diameter.

(3) HPT for powder consolidation through 15 turns showed a unique temperature profile, including an immediate temperature increase at the early stage of HPT for 200 s, followed by a linear increase in temperature through 900 s for $\Delta T = 25$ K. Based on earlier-developed models for general HPT processing of bulk samples, a new temperature rise model for HPT powder consolidation was proposed.

(4) XRD analysis using Williamson-Hall and its modified methods yielded important material parameters of the nanostructured CrMnFeCoNi alloy through 15 HPT turns. Nanoindentation measurements revealed a pronounced strain-rate sensitivity in the HPT-processed alloy. The evaluated activation volumes indicate a significant contribution of grain boundary diffusion–controlled mechanisms as a dominant micromechanical deformation mode in the nanostructured HEA.

(5) The grain boundary diffusion coefficient of the nanostructured CrMnFeCoNi alloy under plastic deformation by nanoindentation was computed. Comparison with published data demonstrates that nanoindentation-induced plastic deformation leads to accelerated grain boundary–mediated diffusion and deformation processes at room temperature in the nanostructured CrMnFeCoNi after HPT powder consolidation.

Supplementary Information

The online version contains supplementary material available at https://doi.org/10.1007/s44492-026-00014-0.

Supplementary file1 (DOCX 3282 KB)

Acknowledgements

The authors acknowledge Tyler Finch for support in density measurements. Laboratory X-ray diffraction has been undertaken at the Institute for Advanced Materials & Manufacturing (IAMM) Diffraction Facility, located at the University of Tennessee, Knoxville. This study was supported in part by the National Science Foundation of the United States under Grant No. CMMI-2051205 (M.K. and M.K.S.) and CMMI-2525114 (M.K.). The authors (K.-D.L. and J.D.N.) gratefully acknowledge support from the U.S. Department of Energy under Assistance Agreement No. DE-EE009177. This research was partly supported by the National Science Foundation Materials Research Science and Engineering Center (MRSEC) program through the UT Knoxville Center for Advanced Materials and Manufacturing (DMR-2309083). The work at Hanyang University was supported by the National Research Foundation of Korea (NRF) grant funded by the Korean government (MSIT) (No. 2022R1A5A1030054 and RS-2026-25478573).

Author contributions

L.B.: Investigation; Formal Analysis
B.R.: Investigation;
T.D.K.: Investigation;
J.D.N.: Investigation;
S.-Y.L.: Investigation;
J.-i.J.: Investigation, Methodology, Writing- Reviewing and Editing;
M.K.S.: Investigation, Methodology, Writing- Reviewing and Editing;
K.-D.L.: Conceptualization, Writing- Reviewing and Editing;
M.K.: Conceptualization, Supervision, Writing- Original Draft

Data availability

No datasets were generated or analysed during the current study.

Declarations

Ethical approval

Not applicable.

Consent to participate

Not applicable.

Consent to publish

Not applicable.

Competing interest

M. Kawasaki serves as the Editor-in-Chief of the Journal of Materials Science: Metallurgy.

Received: 13 May 2026 / Accepted: 23 June 2026
Published online: 10 July 2026

References

Asghari-Rad P, Kim Y, Nguyen NT-C, Kim HS (2020) Fabrication of FeCuNi alloy by mechanical alloying followed by consolidation using high-pressure torsion. J Korean Powder Metall Inst 27(1):1–7. https://doi.org/10.4150/KPMI.2020.27.1.1

Asghari-Rad P, Sathiyamoorthi P, Nguyen NT-C, Zargaran A, Kim TS, Kim HS (2021) A powder-metallurgy-based fabrication route towards achieving high tensile strength with ultra-high ductility in high-entropy alloy. Scripta Mater 190:69–74. https://doi.org/10.1016/j.scriptamat.2020.08.038

Beygelzimer Y, Estrin Y, Mazilkin A, Scherer T, Baretzky B, Hahn H, Kulagin R (2021) Quantifying solid-state mechanical mixing by high-pressure torsion. J Alloys Compd 878:160419. https://doi.org/10.1016/j.jallcom.2021.160419

Beygelzimer Y, Filippov A, Estrin Y (2023) 'Turbulent' shear flow of solids under high-pressure torsion. Philos Mag 103(11):1017–1028. https://doi.org/10.1080/14786435.2023.2180681
Cantor B, Chang ITH, Knight P, Vincent AJB (2004) Microstructural development in equiatomic multicomponent alloys. Mater Sci Eng A 375:213–218. https://doi.org/10.1103/PhysRev.56.978
Cao Y, Wang YB, Alhajeri SN, Liao XZ, Zheng WL, Ringer SP, Langdon TG, Zhu YT (2010) A visualization of shear strain in processing by high-pressure torsion. J Mater Sci 45(3):765–770. https://doi.org/10.1007/s10853-009-3998-2
Cao Y, Kawasaki M, Wang YB, Alhajeri SN, Liao XZ, Zheng WL, Ringer SP, Zhu YT, Langdon TG (2010) Unusual macroscopic shearing patterns observed in metals processed by high-pressure torsion. J Mater Sci 45(17):4545–4553. https://doi.org/10.1007/s10853-010-4485-5
Cao Y, Wang YB, Figueiredo RB, Chang L, Liao XZ, Kawasaki M, Zheng WL, Ringer SP, Langdon TG, Zhu YT (2011) Three-dimensional shear-strain patterns induced by high-pressure torsion and their impact on hardness evolution. Acta Mater 59(10):3903–3914. https://doi.org/10.1016/j.actamat.2011.03.015
Chandan AK, Kishore K, Kawasaki M, Langdon TG, Gubicza J (2026) High-pressure torsion of face-centered cubic multi-principal element alloys: Nanostructuring and its influence on properties. Prog Mater Sci 158:101620. https://doi.org/10.1016/j.pmatsci.2025.101620
Chen B (2024) Progress in additive manufacturing of high-entropy alloys. Materials 17(23):5917. https://doi.org/10.3390/ma17235917
Chen S, Tong Y, Liaw PK (2018) Additive manufacturing of high-entropy alloys: a review. Entropy 20(12):937. https://doi.org/10.3390/e20120937
Choi I-C, Yoo B-G, Kim Y-J, Seok M-Y, Wang Y, Jang J-i (2011) Estimating the stress exponent of nanocrystalline nickel: sharp vs. spherical indentation. Scripta Mater 65(4):300–303. https://doi.org/10.1016/j.scriptamat.2011.04.031
Choi IC, Kim YJ, Wang YM, Ramamurty U, Jang JI (2013) Nanoindentation behavior of nanotwinned Cu: influence of indenter angle on hardness, strain rate sensitivity and activation volume. Acta Mater 61(19):7313–7323. https://doi.org/10.1016/j.actamat.2013.08.037
Choi N, Kulitckii V, Kottke J, Tas B, Choe J, Yu JH, Yang S, Park JH, Lee JS, Wilde G, Divinski SV (2020) Analyzing the 'non-equilibrium state' of grain boundaries in additively manufactured high-entropy CoCrFeMnNi alloy using tracer diffusion measurements. J Alloys Compd 844:155757. https://doi.org/10.1016/j.jallcom.2020.155757
Choi N, da Silva Pinto M, Yang S, Yu JH, Lee J-S, Luckabauer M, Wilde G, Divinski SV (2024) Grain boundary diffusion in additively manufactured CoCrFeMnNi high-entropy alloys: impact of non-equilibrium state, temperature and relaxation. Materialia 38:102228. https://doi.org/10.1016/j.mtla.2024.102228
Christofidou KA, Pickering EJ, Orsatti P, Mignanelli PM, Slater TJA, Stone HJ, Jones NG (2018) On the influence of Mn on the phase stability of the CrMnxFeCoNi high entropy alloys. Intermetallics 92:84–92. https://doi.org/10.1016/j.intermet.2017.09.011
Chulist R, Pukenas A, Chekhonin P, Hohenwarter A, Pippan R, Schell N, Skrotzki W (2022) Phase transformation induced by high pressure torsion in the high-entropy alloy CrMnFeCoNi. Materials (Basel) 15(23):8407. https://doi.org/10.3390/ma15238407
Čížek J, Janeček M, Vlasák T, Smola B, Melikhova O, Islamgaliev RK, Dobatkin SV (2019) The development of vacancies during severe plastic deformation. Mater Trans 60(8):1533–1542. https://doi.org/10.2320/matertrans.MF201937
Conrad H (2003) Grain size dependence of the plastic deformation kinetics in Cu. Mater Sci Eng A 341(1–2):216–228. https://doi.org/10.1016/S0921-5093(02)00238-1
Conrad H (2007) Plastic deformation kinetics in nanocrystalline FCC metals based on the pile-up of dislocations. Nanotechnol 18(32):325701. https://doi.org/10.1088/0957-4484/18/32/325701
Dinita A, Neacsa A, Portoaca AI, Tanase M, Ilinca CN, Ramadan IN (2023) Additive manufacturing post-processing treatments, a review with emphasis on mechanical characteristics. Materials 16(13):4610. https://doi.org/10.3390/ma16134610
Divinski SV, Reglitz G, Wilde G (2010) Grain boundary self-diffusion in polycrystalline nickel of different purity levels. Acta Mater 58(2):386–395. https://doi.org/10.1016/j.actamat.2009.09.015
Divinski SV, Reglitz G, Rösner H, Estrin Y, Wilde G (2011) Ultra-fast diffusion channels in pure Ni severely deformed by equal-channel angular pressing. Acta Mater 59(5):1974–1985. https://doi.org/10.1016/j.actamat.2010.11.063
Edalati K, Miresmaeili R, Horita Z, Kanayama H, Pippan R (2011) Significance of temperature increase in processing by high-pressure torsion. Mater Sci Eng A 528(24):7301–7305. https://doi.org/10.1016/j.msea.2011.06.031
Edalati K, Hashiguchi Y, Pereira PHR, Horita Z, Langdon TG (2018) Effect of temperature rise on microstructural evolution during high-pressure torsion. Mater Sci Eng A 714:167–171. https://doi.org/10.1016/j.msea.2017.12.095
Figueiredo RB, Langdon TG (2021) Deformation mechanisms in ultrafine-grained metals with an emphasis on the Hall-Petch relationship and strain rate sensitivity. J Mater Res Technol 14:137–159. https://doi.org/10.1016/j.jmrt.2021.06.016
Figueiredo RB, Pereira PHR, Aguilar MTP, Cetlin PR, Langdon TG (2012) Using finite element modeling to examine the temperature distribution in quasi-constrained high-pressure torsion. Acta Mater 60(6–7):3190–3198. https://doi.org/10.1016/j.actamat.2012.02.027
Figueiredo RB, Wolf W, Langdon TG (2022) Effect of grain size on strength and strain rate sensitivity in the CrMnFeCoNi high-entropy alloy. J Mater Res Technol 20:2358–2368. https://doi.org/10.1016/j.jmrt.2022.07.181
Figueiredo RB, Kawasaki M, Langdon TG (2023) Seventy years of Hall-Petch, ninety years of superplasticity and a generalized approach to the effect of grain size on flow stress. Prog Mater Sci 137:101131. https://doi.org/10.1016/j.pmatsci.2023.101131
Frost HJ, Ashby MF (1982) Deformation-mechanism maps: the plasticity and creep of metals and ceramics. Pergamon Press, Oxford, New York
George EP, Raabe D, Ritchie RO (2019) High-entropy alloys. Nat Rev Mater 4(8):515–534. https://doi.org/10.1038/s41578-019-0121-4
Gianelle MA, Clapp C, Kundu A, Chan HM (2022) Solid state processing of the cantor derived alloy CoCrFeMnNi by oxide reduction. Res Mater 14:100286. https://doi.org/10.1016/j.rinma.2022.100286
Glienke M, Vaidya M, Gururaj K, Daum L, Tas B, Rogal L, Pradeep KG, Divinski SV, Wilde G (2020) Grain boundary diffusion in CoCrFeMnNi high entropy alloy: kinetic hints towards a phase decomposition. Acta Mater 195:304–316. https://doi.org/10.1016/j.actamat.2020.05.009
Gwalani B, Martin A, Kautz E, Guo B, Lambeets SV, Olszta M, Battu AK, Malakar A, Yang F, Guo J, Thevuthasan S, Li R, Amassian A, Thuo M, Devaraj A (2024) Mechanistic understanding of speciated oxide growth in high entropy alloys. Nat Commun 15(1):5026. https://doi.org/10.1038/s41467-024-49243-8
Han JK, Herndon T, Jang JI, Langdon TG, Kawasaki M (2020) Synthesis of hybrid nanocrystalline alloys by mechanical bonding through high-pressure torsion. Adv Eng Mater 22(4):1901289. https://doi.org/10.1002/adem.201901289
Han JK, Liu XJ, Lee I, Kuzminova YO, Evlashin SA, Liss KD, Kawasaki M (2021) Structural evolution during nanostructuring of additive manufactured 316L stainless steel by high-pressure torsion. Mater Lett 302:130364. https://doi.org/10.1016/j.matlet.2021.130364
Heczel A, Kawasaki M, Lábár JL, Jang J-I, Langdon TG, Gubicza J (2017) Defect structure and hardness in nanocrystalline CoCrFeMnNi high-entropy alloy processed by high-pressure torsion. J Alloys Compd 711:143–154. https://doi.org/10.1016/j.jallcom.2017.03.352
Hernández-Escobar D, Kawasaki M, Boehlert CJ (2021) Metal hybrids processed by high-pressure torsion: synthesis, microstructure, mechanical properties and developing trends. Int Mater Rev 67(3):231–265. https://doi.org/10.1080/09506608.2021.1922807
Hóbor S, Kovács Z, Révész Á (2010) Estimation of heat production during high pressure torsion of Cu-based metallic glass. J Alloys Compd 495(2):352–355. https://doi.org/10.1016/j.jallcom.2009.10.056
Huang M, Jiang J, Wang Y, Dong J, Cui J, Kong L (2024) Integrated manufacturing of powder metallurgy preparation-thixoforming for $Al_{0.8}Co_{0.5}Cr_{1.5}CuFeNi$ HEA: Excellent formability and enhancement by in-situ generated Al_2O_3 in liquid phase. Mater Sci Eng A 916:147289. https://doi.org/10.1016/j.msea.2024.147289
Jiang Y, Liu Y, Zhou H, Taheriniya S, Bian B, Rogal L, Wang JT, Divinski S, Wilde G (2024) Diffusion in ultra-fine-grained CoCrFeNiMn high entropy alloy processed by equal-channel angular pressing. J Mater Sci 59(14):5805–5817. https://doi.org/10.1007/s10853-024-09463-1
Kang YS, Lee JS, Divinski SV, Herzig C (2004) Ni grain boundary diffusion in coarse-grained Fe-40 wt.% Ni alloy and comparison with Ni diffusion in the nanocrystalline alloy. Int J Mater Res 95(2):76–79. https://doi.org/10.3139/ijmr-2004-0018
Karato S-I (2009) Theory of lattice strain in a material undergoing plastic deformation: basic formulation and applications to a cubic crystal. Phys Rev B 79(21):214106. https://doi.org/10.1103/PhysRevB.79.214106
Kawasaki M (2013) Different models of hardness evolution in ultrafine-grained materials processed by high-pressure torsion. J Mater Sci 49(1):18–34. https://doi.org/10.1007/s10853-013-7687-9
Kawasaki M, Ahn B, Kumar P, Jang JI, Langdon TG (2017) Nano-and micro-mechanical properties of ultrafine-grained materials processed by severe plastic

deformation techniques. Adv Eng Mater 19(1). https://doi.org/10.1002/adem.201600578
Kawasaki M, Han JK, Liu XJ, Onuki Y, Kuzminova YO, Evlashin SA, Pesin AM, Zhilyaev AP, Liss KD (2022) In situ heating neutron and X-ray diffraction analyses for revealing structural evolution during postprinting treatments of additive-manufactured 316L stainless steel. Adv Eng Mater 24(4):2100968. https://doi.org/10.1002/adem.202100968
Kawasaki M, Han JK, Liu XJ, Moon SC, Liss KD (2023) Synchrotron high-Energy X-ray & neutron diffraction, and laser-scanning confocal microscopy: In-situ characterization techniques for bulk nanocrystalline metals. Mater Trans 64(8):1683–1694. https://doi.org/10.2320/matertrans.MT-MF2022022
Kilmametov A, Kulagin R, Mazilkin A, Seils S, Boll T, Heilmaier M, Hahn H (2019) High-pressure torsion driven mechanical alloying of CoCrFeMnNi high entropy alloy. Scripta Mater 158:29–33. https://doi.org/10.1016/j.scriptamat.2018.08.031
Kirchheim R (2007) Reducing grain boundary, dislocation line and vacancy formation energies by solute segregation. I. Theoretical background. Acta Mater 55(15):5129–5138. https://doi.org/10.1016/j.actamat.2007.05.047
Korznikov AV, Safarov IM, Laptionok DV, Valiev RZ (1991) Structure and properties of superfine-grained iron compacted out of ultradisperse powder. Acta Metall Mater 39(12):3193–3197. https://doi.org/10.1016/0956-7151(91)90054-5
Kulagin R, Beygelzimer Y, Ivanisenko Y, Mazilkin A, Hahn H (2017) High Pressure torsion: from laminar flow to turbulence. IOP Conf Ser: Mater Sci Eng 194:012045. https://doi.org/10.1088/1757-899x/194/1/012045
Kulagin R, Beygelzimer Y, Iyanisenko Y, Mazilkin A, Straumal B, Hahn H (2018) Instabilities of interfaces between dissimilar metals induced by high pressure torsion. Mater Lett 222:172–175. https://doi.org/10.1016/j.matlet.2018.03.200
Kuzminova YO, Kudryavtsev EA, Han JK, Kawasaki M, Evlashin SA (2021) Phase and structural changes during heat treatment of additive manufactured CrFeCoNi high-entropy alloy. J Alloys Compd 889:161495. https://doi.org/10.1016/j.jallcom.2021.161495
Langdon TG (1994) A unified approach to grain boundary sliding in creep and superplasticity. Acta Metall Mater 42(7):2437–2443. https://doi.org/10.1016/0956-7151(94)90322-0
Laplanche G, Gadaud P, Horst O, Otto F, Eggeler G, George EP (2015) Temperature dependencies of the elastic moduli and thermal expansion coefficient of an equiatomic, single-phase CoCrFeMnNi high-entropy alloy. J Alloys Compd 623:348–353. https://doi.org/10.1016/j.jallcom.2014.11.061
Laplanche G, Bonneville J, Varvenne C, Curtin WA, George EP (2018) Thermal activation parameters of plastic flow reveal deformation mechanisms in the CrMnFeCoNi high-entropy alloy. Acta Mater 143:257–264. https://doi.org/10.1016/j.actamat.2017.10.014
Lee DH, Choi IC, Seok MY, He JY, Lu ZP, Suh JY, Kawasaki M, Langdon TG, Jang JI (2015) Nanomechanical behavior and structural stability of a nanocrystalline CoCrFeNiMn high-entropy alloy processed by high-pressure torsion. J Mater Res 30(18):2804–2815. https://doi.org/10.1557/jmr.2015.239
Lee DH, Choi IC, Yang GH, Lu ZP, Kawasaki M, Ramamurty U, Schwaiger R, Jang JI (2018) Activation energy for plastic flow in nanocrystalline CoCrFeMnNi high-entropy alloy: a high temperature nanoindentation study. Scripta Mater 156:129–133. https://doi.org/10.1016/j.scriptamat.2018.07.014
Lee DH, Choi IC, Kawasaki M, Langdon TG, Jang JI (2023) A review of recent research on nanoindentation of high-entropy alloys processed by high-pressure torsion. Mater Trans 64(7):1551–1565. https://doi.org/10.2320/matertrans.MT-MF2022015
Lee IS, Bhatta L, Xu DH, Blankenburg M, Lienert U, Liss KD, Kawasaki M (2025) Defect-driven relaxation of nanostructured Cu examined by in situ heating high-energy synchrotron X-ray microbeam diffraction. J Alloys Compd 1028:180599. https://doi.org/10.1016/j.jallcom.2025.180599
Li J, Van Vliet KJ, Zhu T, Yip S, Suresh S (2002) Atomistic mechanisms governing elastic limit and incipient plasticity in crystals. Nature 418(6895):307–310. https://doi.org/10.1038/nature00865
Liu C, Jiang X, Sun H, Liu T, Wu Z, Yang L (2023) Preparation of graphene film reinforced CoCrFeNiMn high-entropy alloy matrix composites with strength-plasticity synergy via flake powder metallurgy method. J Mater Res Technol 27:7614–7626. https://doi.org/10.1016/j.jmrt.2023.11.182
Liu XJ, Han JK, Onuki Y, Kuzminova YO, Evlashin SA, Kawasaki M, Liss KD (2023) In situ neutron diffraction investigating microstructure and texture evolution upon heating of nanostructured CoCrFeNi high-entropy alloy. Adv Eng Mater 25(6):2201256. https://doi.org/10.1002/adem.202201256
Miracle DB, Senkov ON (2017) A critical review of high entropy alloys and related concepts. Acta Mater 122:448–511. https://doi.org/10.1016/j.actamat.2016.08.081
Mohammadi A, Edalati P, Arita M, Bae JW, Kim HS, Edalati K (2022) Microstructure and defect effects on strength and hydrogen embrittlement of high-entropy alloy CrMnFeCoNi processed by high-pressure torsion. Mater Sci Eng A 844:143179. https://doi.org/10.1016/j.msea.2022.143179
Oketola AM, Adegbola TA, Jamiru T, Ogunbiyi O, Salifu S (2025) Advances in high-entropy alloy research: unraveling fabrication techniques, microstructural transformations, and mechanical properties. J Bio- Tribo-Corros 11(3):79. https://doi.org/10.1007/s40735-025-00999-6
Oliver WC, Pharr GM (2011) An improved technique for determining hardness and elastic modulus using load and displacement sensing indentation experiments. J Mater Res 7(6):1564–1583. https://doi.org/10.1557/jmr.1992.1564
Patterson AL (1939) The scherrer formula for X-ray particle size determination. Phys Rev 56(10):978–982. https://doi.org/10.1103/PhysRev.56.978
Pereira PHR, Figueiredo RB, Huang Y, Cetlin PR, Langdon TG (2014) Modeling the temperature rise in high-pressure torsion. Mater Sci Eng A 593:185–188. https://doi.org/10.1016/j.msea.2013.11.015
Pickering EJ, Jones NG (2016) High-entropy alloys: a critical assessment of their founding principles and future prospects. Int Mater Rev 61(3):183–202. https://doi.org/10.1080/09506608.2016.1180020
Reis LM, Hohenwarter A, Kawasaki M, Figueiredo RB (2024) Evaluating high-pressure torsion scale-up. Adv Eng Mater 26(19):2400175. https://doi.org/10.1002/adem.202400175
Sauvage X, Wilde G, Divinski SV, Horita Z, Valiev RZ (2012) Grain boundaries in ultrafine grained materials processed by severe plastic deformation and related phenomena. Mater Sci Eng A 540:1–12. https://doi.org/10.1016/j.msea.2012.01.080
Schuh B, Mendez-Martin F, Völker B, George EP, Clemens H, Pippan R, Hohenwarter A (2015) Mechanical properties, microstructure and thermal stability of a nanocrystalline CoCrFeMnNi high-entropy alloy after severe plastic deformation. Acta Mater 96:258–268. https://doi.org/10.1016/j.actamat.2015.06.025
Shahmir H, He JY, Lu ZP, Kawasaki M, Langdon TG (2016) Effect of annealing on mechanical properties of a nanocrystalline CoCrFeNiMn high-entropy alloy processed by high-pressure torsion. Mater Sci Eng A 676:294–303. https://doi.org/10.1016/j.msea.2016.08.118
Skrotzki W, Pukenas A, Odor E, Joni B, Ungar T, Völker B, Hohenwarter A, Pippan R, George EP (2020) Microstructure, texture, and strength development during high-pressure torsion of CrMnFeCoNi high-entropy alloy. Crystals (Basel) 10(4):336. https://doi.org/10.3390/cryst10040336
Son S, Asghari-Rad P, Zargaran A, Chen W, Kim HS (2022) Superlative room temperature and cryogenic tensile properties of nanostructured CoCrFeNi medium-entropy alloy fabricated by powder high-pressure torsion. Scripta Mater 213:114631. https://doi.org/10.1016/j.scriptamat.2022.114631
Stückler M, Weissitsch L, Wurster S, Krenn H, Pippan R, Bachmaier A (2021) Sampling the Cu–Fe–Co phase diagram by severe plastic deformation for enhanced soft magnetic properties. J Mater Res Technol 12:1235–1242. https://doi.org/10.1016/j.jmrt.2021.03.073
Thompson AW (1972) Calculation of true volume grain diameter. Metallogr 5(4):366–369. https://doi.org/10.1016/0026-0800(72)90018-3
Ungár T, Ott S, Sanders PG, Borbély A, Weertman JR (1998) Dislocations, grain size and planar faults in nanostructured copper determined by high resolution X-ray diffraction and a new procedure of peak profile analysis. Acta Mater 46(10):3693–3699. https://doi.org/10.1016/S1359-6454(98)00001-9
Ungar T, Dragomir I, Revesz A, Borbely A (1999) The contrast factors of dislocations in cubic crystals: the dislocation model of strain anisotropy in practice. J Appl Crystallogr 32(5):992–1002. https://doi.org/10.1107/S0021889899009334
Vaidya M, Pradeep KG, Murty BS, Wilde G, Divinski SV (2017) Radioactive isotopes reveal a non sluggish kinetics of grain boundary diffusion in high entropy alloys. Sci Rep 7(1):12293. https://doi.org/10.1038/s41598-017-12551-9
Valiev RZ, Mishra RS, Groza J, Mukherjee AK (1996) Processing of nanostructured nickel by severe plastic deformation consolidation of ball-milled powder. Scripta Mater 34(9):1443–1448. https://doi.org/10.1016/1359-6462(95)00676-1
Valiev RZ, Estrin Y, Horita Z, Langdon TG, Zehetbauer MJ, Zhu YT (2006) Producing bulk ultrafine-grained materials by severe plastic deformation. JOM 58(4):33–39. https://doi.org/10.1007/s11837-006-0213-7
Valiev RZ, Estrin Y, Horita Z, Langdon TG, Zehetbauer MJ, Zhu YT (2016) Producing bulk ultrafine-grained materials by severe plastic deformation: ten years later. JOM 68(4):1216–1226. https://doi.org/10.1007/s11837-016-1820-6
Valiev RZ, Alexandrov IV, Kawasaki M, Langdon TG (2024) Ultrafine-grained materials. In: Valiev RZ, Alexandrov IV, Kawasaki M, Langdon TG (eds) Ultrafine-grained materials, Springer International Publishing, Cham. https://doi.org/10.1007/978-3-031-31729-3

Wang CL, Lai YH, Huang JC, Nieh TG (2010) Creep of nanocrystalline nickel: a direct comparison between uniaxial and nanoindentation creep. Scripta Mater 62(4):175–178. https://doi.org/10.1016/j.scriptamat.2009.10.021

Wilkens M (1970) The determination of density and distribution of dislocations in deformed single crystals from broadened X-ray diffraction profiles. Phys Status Solidi A 2(2):359–370. https://doi.org/10.1002/pssa.19700020224

Wu Y, Liu WH, Wang XL, Ma D, Stoica AD, Nieh TG, He ZB, Lu ZP (2014) In-situ neutron diffraction study of deformation behavior of a multi-component high-entropy alloy. Appl Phys Lett 104(5):051910. https://doi.org/10.1063/1.4863748

Wu Z, Bei H, Pharr GM, George EP (2014) Temperature dependence of the mechanical properties of equiatomic solid solution alloys with face-centered cubic crystal structures. Acta Mater 81:428–441. https://doi.org/10.1016/j.actamat.2014.08.026

Wu Y-H, Bhatta L, Lee I, Figueiredo RB, Kawasaki M, Santala MK (2024) Multi-scale characterization of supersaturated and intermetallic nanoscale phases in alloys produced by high-pressure torsion processing of Al and Mg sheets. JOM 77(3):1233–1240. https://doi.org/10.1007/s11837-024-07064-6

Wu Y-H, Lee I, Bhatta L, Figueiredo RB, Kawasaki M, Santala MK (2026) Microstructural characterization and mechanical properties of Al-1043 produced by cold angular roll processing. Mater Charact 232:116006. https://doi.org/10.1016/j.matchar.2026.116006

Yeh JW, Chen SK, Lin SJ, Gan JY, Chin TS, Shun TT, Tsau CH, Chang SY (2004) Nanostructured high-entropy alloys with multiple principal elements: novel alloy design concepts and outcomes. Adv Eng Mater 6(5):299–303. https://doi.org/10.1002/adem.200300567

Zamani MR, Mirzadeh H, Malekan M, Cao SC, Yeh J-W (2022) Grain growth in high-entropy alloys (HEAs): a review. High Entropy Alloys Mater 1(1):25–59. https://doi.org/10.1007/s44210-022-00002-8

Zhang Y, Zuo TT, Tang Z, Gao MC, Dahmen KA, Liaw PK, Lu ZP (2014) Microstructures and properties of high-entropy alloys. Prog Mater Sci 61:1–93. https://doi.org/10.1016/j.pmatsci.2013.10.001

Zhang B, Huang Y, Dou Z, Wang J, Huang Z (2024) Refractory high-entropy alloys fabricated by powder metallurgy: progress, challenges and opportunities. J Sci Adv Mater Devices 9(2):100688. https://doi.org/10.1016/j.jsamd.2024.100688

Zhao WR, Han JK, Kuzminova YO, Evlashin SA, Zhilyaev AP, Pesin AM, Jang JI, Liss KD, Kawasaki M (2021) Significance of grain refinement on micro-mechanical properties and structures of additively-manufactured CoCrFeNi high-entropy alloy. Mater Sci Eng A 807:140898. https://doi.org/10.1016/j.msea.2021.140898

Zhao YK, Park JM, Murakami K, Komazaki S, Kawasaki M, Tsuchiya K, Suh JY, Ramamurty U, Jang JI (2021b) Exploring the hydrogen absorption and strengthening behavior in nanocrystalline face-centered cubic high-entropy alloys. Scripta Mater 203. https://doi.org/10.1016/j.scriptamat.2021.114069

Zhilyaev AP, Langdon TG (2008) Using high-pressure torsion for metal processing: fundamentals and applications. Prog Mater Sci 53(6):893–979. https://doi.org/10.1016/j.pmatsci.2008.03.002

Zhu T, Li J, Samanta A, Kim HG, Suresh S (2007) Interfacial plasticity governs strain rate sensitivity and ductility in nanostructured metals. Proc Natl Acad Sci U S A 104(9):3031–3036. https://doi.org/10.1073/pnas.0611097104

Publisher's Note